

Computer Methods in Biomechanics and Biomedical Engineering


ISSN: 1025-5842 (Print) 1476-8259 (Online) Journal homepage: <http://www.tandfonline.com/loi/gcmb20>


A nonlinear anisotropic inverse method for computational dissection of inhomogeneous planar tissues

Colleen M. Witzenburg & Victor H. Barocas


To cite this article: Colleen M. Witzenburg & Victor H. Barocas (2016): A nonlinear anisotropic inverse method for computational dissection of inhomogeneous planar tissues, Computer Methods in Biomechanics and Biomedical Engineering, DOI: [10.1080/10255842.2016.1176154](https://doi.org/10.1080/10255842.2016.1176154)

To link to this article: <http://dx.doi.org/10.1080/10255842.2016.1176154>

 View supplementary material 

 Published online: 02 May 2016.

 Submit your article to this journal 

 Article views: 37

 View related articles 

 View Crossmark data 

A nonlinear anisotropic inverse method for computational dissection of inhomogeneous planar tissues

Colleen M. Witzenburg^a and Victor H. Barocas^b

^aDepartment of Mechanical Engineering, University of Minnesota, Minneapolis, MN, USA; ^bDepartment of Biomedical Engineering, University of Minnesota, Minneapolis, MN, USA

ABSTRACT

Quantification of the mechanical behavior of soft tissues is challenging due to their anisotropic, heterogeneous, and nonlinear nature. We present a method for the 'computational dissection' of a tissue, by which we mean the use of computational tools both to identify and to analyze regions within a tissue sample that have different mechanical properties. The approach employs an inverse technique applied to a series of planar biaxial experimental protocols. The aggregated data from multiple protocols provide the basis for (1) segmentation of the tissue into regions of similar properties, (2) linear analysis for the small-strain behavior, assuming uniform, linear, anisotropic behavior within each region, (3) subsequent nonlinear analysis following each individual experimental protocol path and using local linear properties, and (4) construction of a strain energy data set $W(E)$ at every point in the material by integrating the differential stress-strain functions along each strain path. The approach has been applied to simulated data and captures not only the general nonlinear behavior but also the regional differences introduced into the simulated tissue sample.

ARTICLE HISTORY

Received 5 September 2015
Accepted 5 April 2016

KEYWORDS

Biaxial testing; biomechanics; elastography; heterogeneity; subdomain

Introduction

Soft tissues (e.g. tendons, ligaments, articular cartilage, muscle, blood vessels, heart valve leaflets, etc.) are essential for function as they provide support and protection as well as transmitting forces throughout the body. The mechanical behavior of soft tissues is fundamentally linked to their composition, in particular to the concentration and arrangement of the structural extracellular constituents (e.g. collagen, elastin, proteoglycans). In general, soft tissues exhibit directional-dependent behavior that correlates strongly with the anisotropic arrangement of their fibrous extracellular matrix. Soft tissues are often inhomogeneous. The presence and proportions of the structural extracellular constituents as well as their arrangement and alignment vary locally, causing regional differences in both anisotropy and stiffness. The heterogeneous nature of soft tissues becomes particularly evident at insertion or connection points (Thomopoulos et al. 2006) and in cases of disease or injury. Finally, their stress-strain behavior is often strongly nonlinear, particularly at the high strain levels that occur physiologically. The intrinsic complexity

of soft tissues thus presents a tremendous challenge in constitutive modeling.

There have been many studies aimed at quantifying the properties of soft tissues. Elastography has become a major focus for medical imaging (Ophir et al. 1996; Greenleaf et al. 2003; Ehman et al. 2012) as it has the potential to provide *in vivo* information. In static elastography, the tissue is compressed or elongated slowly, and the distribution of its displacement is captured (e.g. with MR, ultrasound, acoustic or optically) and interpreted. Dynamic elastography involves the application of time-harmonic motion. MR and ultrasound have produced full 3D reconstructions of displacement fields within tissues from multiple slices of 2D displacement information, induced by harmonic excitations and are widely used to detect tumors in the breast, prostate, liver, etc. (Manduca et al. 2001; Sinkus et al. 2008; Perumpail et al. 2012). Though they assumed isotropy, the nonlinear inverse elasticity method of Oberai, Barbone, and colleagues (Gokhale et al. 2008; Goenezen et al. 2011; Goenezen et al. 2012; Tyagi et al. 2014) is perhaps the most compelling at determining heterogeneity. In their study

of breast cancer tumors, the size, shape, and location of regions within a tissue sample with varying shear moduli were identified with exceptional clarity. While traditionally non-invasive imaging-based approaches assume linear, isotropic material behavior, they are beginning to be used to estimate anisotropic properties. For example, Tweten et al. (2015) developed a method using MR elastography to quantify the material properties of transversely isotropic soft tissue using shear waves with specific polarization and propagation directions. The same group also developed an extended local frequency estimation inversion scheme for anisotropic materials (Clayton et al. 2013). However, in both cases though the material is anisotropic, the fiber direction must be known *a priori*.

Typically, tissues are tested mechanically *in vitro* using indentation, inflation, and/or biaxial tension. Indentation has been applied to determine heterogeneity through its controlled and repeated application. Most indentation-based methods assume linearity (infinitesimal deformation) and isotropy, but a few have been modified to account for the anisotropic, nonlinear behavior strongly exhibited by soft tissues. For example, utilizing atomic force microscopy, Costa and Yin (1999) investigated the effects of indenter geometry, nonlinear material behavior, and large deformations on soft tissues locally, gathering in-depth information regarding tissue heterogeneity, but they did not include anisotropy in their analysis. Cox et al. (2008), developed an indentation method capable of capturing anisotropy by combining force and deformation gradient data (captured through an inverted confocal microscope). They utilized repeated indentation to quantify the inhomogeneous nature of the heart valve leaflet (Cox et al. 2010), which they coupled with inverse finite element analysis using a mixed numerical approach to determine local material properties. Nonlinearity was incorporated using the constitutive framework of Holzapfel et al. (2000). Chai et al. (2013) and Chai et al. (2014) further utilized the methods of Cox to characterize the heterogeneous properties of atherosclerotic plaques, focusing on the drastic differences in the material properties of the various plaque components using a sophisticated inverse finite element method. Other approaches for extracting anisotropic material properties via indentation involve the use of simultaneous indentation and stretch (Karduna et al. 1997) and an indenter with asymmetric geometry (Bischoff 2004). Nonlinearity is typically incorporated numerically, but has also been incorporated analytically as per Humphrey et al. (1991). Although indentation is attractive in that it can be applied to a tissue specimen locally in a controlled and repeatable manner, it is less relevant to *in vivo* function for many tissues.

Inflation (Schulze-Bauer et al. 2002; Saravanan et al. 2006; Boyce et al. 2008) is often a more realistic loading modality. The inverse method proposed by Seshaiyer and Humphrey (2003) incorporates nonlinearity, anisotropy, and heterogeneity but requires a fully integrated finite element model. Seshaiyer utilized the principle of virtual work and a computationally demanding Marquardt–Levenberg regression scheme to determine the best-fit values of the material parameters. The method was utilized successfully in the quantification of the material properties of the lens capsule (Pedrigi et al. 2007) but was limited to small regions of interest within the tissue. Kroon and Holzapfel (2008) propose an alternative inverse method, which enabled the investigation of the distribution of anisotropic material properties. A pointwise identification method for the determination of heterogeneous, nonlinear properties of cerebral aneurysms was proposed (Lu & Zhao 2009), validated (Zhao et al. 2009), and applied to patient specific geometries (Zhao et al. 2011) by Lu and Zhao. Though inflation is often the most physiologic testing mode, it must be applied globally to a tissue specimen. As such, it is difficult to interrogate a region of the tissue under a wide range of strain states and in particular to shear the tissue, and the material constants determined are often only applicable for the strain state studied.

Planar extension allows for the investigation of the multiaxial behavior of the tissue and the introduction of shear. Soft tissues, however, often have an inelastic response, exhibiting hysteresis between the loading and unloading stress–strain behavior. If material behavior from multiple loading configurations is to be combined properly, some form of preconditioning must be applied such that pseudo-elasticity can be reasonably applied. Nielsen and colleagues (Malcolm et al. 2002; Nielsen et al. 2002) built a one-of-a-kind multiaxial tester to capture the mechanical behavior of anisotropic, heterogeneous tissues and verified their deformation measurement technique on an inhomogeneous rubber membrane and on a sheep diaphragm. In more recent work by the same group (Flynn et al. 2011; Flynn et al. 2013), multiple loading configurations encompassing both indentation and shear were used to investigate the properties of skin. The Tong and Fung model was fit to the data (errors ranging from ~13 to 22%), but the heterogeneity of the tissue was not investigated. Flynn et al. (1998) present an elegant inverse method to determine anisotropic, nonlinear properties of planar soft tissues subjected to a variety of biaxial loading conditions that encompass both tension and shear. They utilize the tangent stiffness along with an incremental force-displacement approach to capture the nonlinear behavior of the tissue. The main drawback of Flynn's approach is the need to test multiple specimens from different physical locations to investigate heterogeneity.

Uniaxial and biaxial testing has been completed on small samples cut from different sections of myocardium (Demer & Yin 1983; Sacks & Chuong 1993; Novak et al. 1994; Ghaemi et al. 2009), supraspinatus tendon (Huang et al. 2005; Lake et al. 2009, 2010; Szczesny et al. 2012), and aorta (Sokolis et al. 2008; Pasta et al. 2012) to determine regional variation. While this approach has yielded valuable information, again it is hindered by dissection damage, minimal testable sample size, and the need to treat each individual sample as homogeneous.

In addition to the experimental challenges, the complex structure and mechanical behavior of soft tissues make selecting, applying, and fitting an appropriate constitutive relation difficult. There are many prominent strain energy functions which have been developed to capture both the anisotropy and nonlinearity of various soft tissues including Fung-type, neo-Hookean, Mooney–Rivlin, and Ogden relations (Fung 1993; Holzapfel 2000; Humphrey 2002). Selecting (or in some cases developing) an appropriate constitutive relation is not trivial. Humphrey (1999) compared various relations by applying them to the same data set and found that they strongly differed (sometimes reversed) in their descriptions of the tissue in terms of both stiffness and anisotropy, reinforcing the idea that even highly successful constitutive relations are limited in their predictive capabilities. This concern led to a key principle of our inverse approach: instead of selecting a strain energy function and fitting the material parameters to experimental data, one can use experimental data directly to determine the strain energy function.

In our previous work (Raghupathy & Barocas 2010; Raghupathy et al. 2011), we presented the Generalized Anisotropic Inverse Mechanics (GAIM) method to determine the material properties of anisotropic, heterogeneous, linear soft tissues. GAIM uses the measured displacement field over the entire sample as well as the traction forces on the sample boundary to solve the Cauchy stress balance directly for the unknown components of a general linear elasticity tensor. Heterogeneity is managed using a subdomain technique; the sample area is segmented into many partitions, each assumed to have uniform properties. In this way, the method is capable of determining the distribution of material parameters, that is how stiffness and anisotropy change from region to region and whether these changes are drastic and abrupt or more gradual. The linear constitutive equation was replaced with a neo-Hookean form (Witzenburg et al. 2012) to accommodate the large-deformation *kinematics* exhibited by many soft tissues, but the base assumption of linear *kinetics* remained a serious weakness.

One possible approach to tissue nonlinearity would be to replace the neo-Hookean constitutive law with a higher-order constitutive equation. For example, Tonuk and

Silver-Thorn (2003) fit their experimental results using a James–Green–Simpson nonlinear elastic material model. The use of high-order constitutive equations however, typically requires additional assumptions about the material (isotropy and homogeneity in the case of Tönük and Silver-Thorn) lest a prohibitive number of independent material coefficients arise. Our preference is to maintain the maximum amount of flexibility in the constitutive form. In addition, the complexity of the relation increases computation time, sacrificing the tremendous efficiency advantage that comes from the constitutive law being linear with respect to the model parameters. Therefore, while still accounting for the nonlinear kinematics of the deformation as a whole, we approach the problem by considering the mechanical behavior of the tissue in linear increments.

Although the inverse techniques discussed have proven successful in many cases, the Nonlinear Generalized Anisotropic Inverse Mechanics (NGAIM) method proposed here addresses appreciable gaps in current combined capability. The NGAIM method is capable of (1) characterizing anisotropic materials, (2) considering the heterogeneous nature of the tissue, (3) incorporating behavior from many physiologically relevant biaxial loading modalities, (4) accounting for both the nonlinear kinetics and kinematics of soft tissues, and (5) performing without the high computational cost associated with repeated forward solutions. In addition, NGAIM addresses the full behavior of the material, solving for the full-field stress and full-field strain energy within the tissue sample.

Methods

Overall strategy

The novelty of the GAIM method was to solve the weak form of the Cauchy stress balance directly for the mechanical properties of the tissue rather than guessing a set of parameters, performing repeated forward solves, and iterating to determine the best parameter values. While GAIM was capable of describing heterogeneous, anisotropic materials it assumed linearity. Following the historical approach of linearization (Hughes & Pister 1978; Ogden 1984), we chose to capitalize on GAIM by applying it in a stepwise manner in order to capture the behavior of nonlinear materials. Again, the full-field displacement and boundary traction information from multiple biaxial extensions was needed. Due to the changing reference configuration, the initial step (small strain) and the following steps (large strain) are handled differently. However, the material descriptions from each step of each experimental protocol (as described below) are eventually combined to generate a six-dimensional point

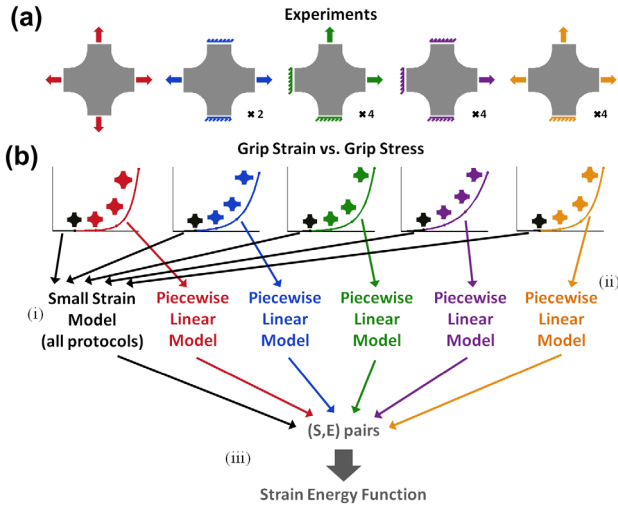


Figure 1. Schematic of method. (a) A set of different biaxial experimental protocols is performed on the sample, providing the displacement fields and grip forces. (b) The analysis includes the following steps: (i) Combined data from all of the protocols at small-strain (black segments in grip force vs. grip strain plots) are used to specify a small-strain model using our previous linear approach (Witzenburg et al. 2012). (ii) Data from each individual protocol at larger strain (colored segments in grip force vs. grip strain plots) are used to generate a piecewise linear model for the protocol's strain path. (iii) The models are used to calculate the PK2 stress at each strain value for each experimental protocol. The PK2 stress is integrated along each strain path to generate the strain energy density value at each strain value. Calculations for the small strain model are by partition, determined using the deformation field per (Witzenburg et al. 2016), and those in the piecewise linear models are by element, so the strain energy density data set is obtained for each element.

cloud of stress-strain data for every sample subregion. Accordingly, any strain-energy density function could then be independently fit quickly and easily to each subregion, thereby fully characterizing its behavior.

The process begins with data generated from an extensive biaxial loading protocol. The more and varied the loading protocol, the wider the region of strain-space investigated for each location in the sample. For a biaxial test, each arm can be extended independently, leading to the 15 permutations shown in Figure 1(a); while this combination of experimental protocols is by no means exhaustive (e.g. a 2:1 ratio of stretch in the two directions could also be performed, Vande Geest et al. 2006), it provides a broad range of deformations. For the current study, the 15 protocols in Figure 1(a) were simulated. Shear in the arms and central region of the sample was achieved through the asymmetric stretches. The experimental procedure would be in the following form. Both the normal and shear forces at the grip would be measured by six-degree-of-freedom load cells (JR3 Inc.). During each extension, a video of the sample surface would provide the full-field deformation

via digital image correlation (DIC) as described elsewhere (Raghupathy 2011). Finally, nodal displacements and arm forces would be extracted from the raw data and step size would be determined. The determination of step size is an important consideration (detailed in Appendix 1) because large steps lose linearity but small steps are more vulnerable to noise effects.

The analysis process is completed in three phases:

- (i) small-strain analysis of the early stages of all experimental protocols was done simultaneously,
- (ii) large-strain analysis was done following each individual experimental protocol path, and
- (iii) an elemental strain energy density data set was generated.

Figure 1(b) shows a schematic of the process; for clarity, only the normal force on a single arm is shown and the step size is exaggerated. A detailed example illustrating the method on a simulated sample is given in the supplementary material.

(i) Small-strain analysis of all experimental protocols simultaneously

For the first step (Figure 1(b-(i))), the raw displacement and force data from all loading protocols were combined per our previous neo-Hookean approach (Witzenburg et al. 2012), creating a general, anisotropic, inhomogeneous *linear* model of the material behavior at small strain. Partitioning the sample into homogenous subdomains, one of the most difficult obstacles in applying GAIM, was done by identifying deformation gradient jumps within the sample under symmetric loading conditions (Witzenburg et al. 2016). As described by (Raghupathy & Barocas 2010) elements are grouped into homogeneous subdomains to ensure that the inverse problem is well-posed. Then, following (Witzenburg, et al. 2012), the force and displacement data for the first step from all 15 extensions were considered simultaneously, and an analogous neo-Hookean generalization of the linear elasticity tensor, K , was determined for each subdomain such that the second Piola-Kirchhoff (PK2) stress, S , was defined by

$$S_{ij} = K_{ijkl} E_{kl} \quad (1)$$

where E is the Green strain, and K is constant over each partition. K was determined by solving the Cauchy stress balance

$$\left(F_{mi} K_{ijkl} E_{kl} \right)_j = 0 \quad (2)$$

where F is the deformation gradient tensor and differentiation is with respect to the undeformed coordinates. In Equation (2), F and E are known from the DIC, allowing K to be determined directly. Following the Galerkin

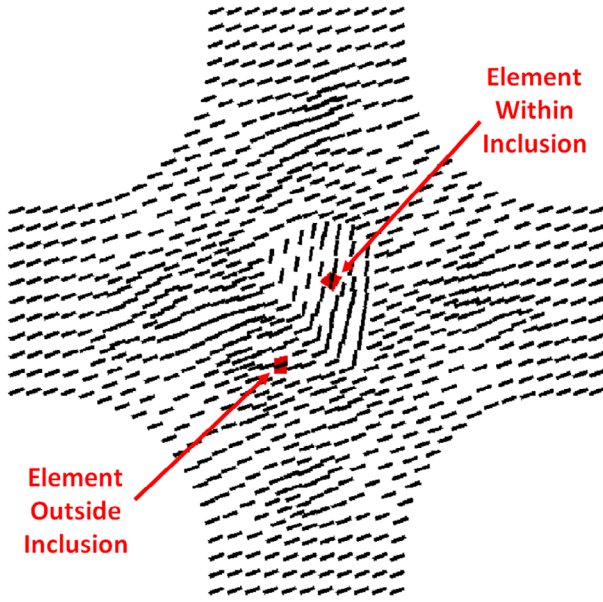


Figure 2. Fiber alignment for the simulated sample with an inclusion oriented at a different angle ($\mu_{\text{inclusion}} = 80^\circ$) than the majority of the sample ($\mu = 20^\circ$). In addition, elements selected for further analysis (an element within the inclusion and an element just outside the inclusion) are highlighted. Simulation parameters, strength of alignment ($\kappa = 1.5$), stiffness ($A = 5 \text{ kPa}$), and nonlinearity ($B = 12$), were set to match fits of the closed-form nonlinear fiber-based structural model to soft tissues.

finite element method, the weak form of Equation (2) for a sample with undeformed domain Ω_0 and boundary Γ_0 is (Raghupathy & Barocas 2010)

$$\sum_e \left(\int_{\Gamma_0^e} t_i N_A d\Gamma_0^e \right) = \sum_e \left(\int_{\Omega_0^e} F_{im} K_{mjqr} E_{qr} N_{A,j} d\Omega_0^e \right) \quad (3)$$

where N_A are the Galerkin basis functions at node A of the finite element, t_i is the traction vector, and the summation is over all elements, e . The force on each grip arm is the total force over the sample boundary, allowing evaluation of the traction integral.

(ii) Large-strain analysis following each individual experimental protocol path

For larger strains (Figure 1(b-(ii))), data from each individual protocol were used to generate a piecewise linear model of the material in the element following the protocol's experimental strain path. It would be attractive simply to continue to apply GAIM to all steps in the same manner, but as Flynn et al. (1998) noted, there is an issue with reference configuration. Consider a point within the material. At the beginning of step 1, the sample is undeformed, and this point is in the same state no matter

what extension is about to be imposed. In other words, because the initial state for the first step of *any* protocol is the tissue's undeformed state, all experimental protocols can be analyzed simultaneously for their first step. At the end of step 1 and thus the beginning of step 2, however, the point has moved, and the location of the point is thus dependent on which loading protocol is being imposed. The reference configuration for the second step is not the same for all protocols. The rationale for the extensive loading scheme is to ensure that the inverse problem is well-posed because it is not possible to determine the material characteristics of a subdomain within the sample without interrogating it under various loading conditions. If GAIM were applied in a stepwise fashion, however, it would no longer be sound to apply the displacement fields and reaction forces from the protocols concurrently. Flynn et al. (1998) addressed this issue elegantly by means of an extensive incremental loading paradigm that allowed for the establishment of multiple reference configurations. Flynn's technique was highly effective for their homogeneous samples, but it required a 3-fold increase in the number of loading cycles applied to the tissue (increasing their loading scheme from 4 cycles to 12 cycles). Given the larger number of 15 loading cycles required to probe the heterogeneous tissues of interest to us, we have selected to consider all subsequent steps in each protocol separately.

The creation of a separate inverse problem for each experimental protocol changes the nature of the problem: the initial NGAIM step is *overdetermined* due to the large number of loading protocols and the relatively small number of partitions; subsequent steps are *underdetermined* since each element and loading protocol are evaluated separately. Unfortunately, the grouping of elements into the deformation gradient-jump determined subregions no longer ensures that each much smaller system of equations is overdetermined. Thus, rather than grouping these subregions into even larger partitions each element within the sample domain was considered a separate material. An alternative additional constraint must therefore be imposed on the matrix problem to achieve well-posedness. We chose to require that K satisfy the discrete stress balance *and* vary least from the K tensor determined for the previous step. The differential PK2 stress, \mathbb{S} , for step n is equal to

$$\mathbb{S}_{ij}^n = \mathbb{K}_{ijkl}^n \mathbb{E}_{ij}^n \quad (4)$$

where \mathbb{K} (differential neo-Hookean elasticity tensor) and \mathbb{E} (differential Green strain) are relative to the sample configuration at the end of step $n - 1$. The differential stresses are additive, meaning that

$$\mathbb{S}_{ij}^N = \sum_{n=1}^N \mathbb{S}_{ij}^n \quad (5)$$

where S_{ij}^N is the PK2 stress in reference to the global undeformed sample configuration at the end of step N , and the PK2 stress for the first step is determined from the small-strain analysis. Because of the nonlinearity of large-strain kinematics, however, strain is *not* additive, (i.e. for $N > 1$, $E_{ij}^N \neq \sum_{n=1}^N E_{ij}^n$). The finite element discretized form of Equation (3), is

$$\sum_e \left(\int_{\Gamma_0^e} t_i^N N_A d\Gamma_0^e \right) = \sum_e \left(\int_{\Omega_0^e} F_{im}^N \left(\sum_{n=1}^N \mathbb{K}_{mjqr}^n E_{qr}^n \right) N_{A,j} d\Omega_0^e \right) \quad (6)$$

The stress summation can be restated in terms of the known and unknown \mathbb{K}_{mjqr} values:

$$\sum_e \left(\int_{\Gamma_0^e} t_i^N N_A d\Gamma_0^e - \int_{\Omega_0^e} F_{im}^N \left(\sum_{n=1}^{N-1} \mathbb{K}_{mjqr}^n E_{qr}^n \right) N_{A,j} d\Omega_0^e \right) = \sum_e \left(\int_{\Omega_0^e} F_{im}^N \mathbb{K}_{mjqr}^N E_{qr}^N N_{A,j} d\Omega_0^e \right) \quad (7)$$

At step N , the LHS of Equation (7) is entirely known, and the RHS contains the unknown \mathbb{K}_{mjqr}^N . Under the assumption that \mathbb{K}_{mjqr} is constant over each element, the equation leads to a new global linear matrix equation for all steps beyond the first of the form

$$\mathcal{F}^N - \sum_{n=1}^{N-1} M^n \mathcal{K}^n = M^N \mathcal{K}^N \quad (8)$$

where M is a matrix consisting of the terms that remain when the material parameter terms on the RHS of Equation (7) are factored out (defined in supplementary material). As stated above, rather than minimizing a residual force norm, the change in the differential neo-Hookean elasticity tensor, $\mathcal{K}^N - \mathcal{K}^{N-1}$, is minimized subject to the constraint that the residual force norm of Equation (8) be zero.

(iii) Generating an elemental constitutive and strain energy data set

The solution of the global matrix equation at each step of each protocol yields a unique differential neo-Hookean elasticity tensor for each subregion (small-strain) or element (large-strain) within the sample domain. The PK2 stress was obtained from those tensors using Equations (4) and (5). By combining all the PK2 stresses calculated over all segments of all protocols for an element along with the corresponding Green strain, a set of ordered pairs, (E, S) , was generated for each element; essentially, each set of pairs (E, S) function as a mechanical characterization of its element as a unique material (Figure 1(b-(iii))).

For a hyperelastic material, the work necessary to deform a body is its intrinsic strain energy density, $W = \int S_{ij} dE_{ij}$. In the case of the piecewise linear model,

the integration was approximated by a summation (trapezoid rule),

$$W_N^p = \sum_{k=0}^N \frac{(S_{ij}^{k+1} + S_{ij}^k)}{2} (E_{ij}^{k+1} - E_{ij}^k) \quad (9)$$

where W_N^p is the strain energy at step N for loading protocol p for an element within the sample domain. In this way, a unique strain energy density data set was generated for each element within the sample domain. The new step-wise method is referred to as the Nonlinear Generalized Anisotropic Inverse Mechanics method or the NGAIM method.

Computational experiments

The NGAIM method was applied to simulations of biaxial extensions generated based on a closed-form nonlinear fiber-based structural model for soft tissues that we have used previously (Raghupathy & Barocas 2009; Witzenburg et al. 2016). Briefly, it considers contributions from a population of fibers in which the constituents are assumed to deform affinely and stresses are assumed to be additive. The fiber population is represented by a bidirectional von Mises distribution,

$$f(\theta; \kappa, \mu) = \frac{1}{\pi I_0(\kappa)} \exp\{\kappa \cos[2(\theta - \mu)]\}, \quad \theta \in [0, \pi) \quad (10)$$

where κ signifies the degree of anisotropy, and μ is the preferred fiber direction. The constitutive equation for the fiber is an exponential form based on the Green strain,

$$S_f = A \left\{ \exp \left[B \left(\lambda_f^2 - 1 \right) \right] - 1 \right\} \quad (11)$$

where λ_f is the fiber stretch for a fiber aligned with angle θ and S_f is the second Piola–Kirchhoff stress in the fiber. The constants A and B capture the overall stiffness and nonlinearity of the fiber response, respectively. If A increases, the fiber is stiffer at all strain levels, and if B increases, the fiber stress–strain response becomes more nonlinear. The overall stress within the tissue is the sum of all the fiber stresses. Strength of alignment ($\kappa = 1.5$), stiffness ($A = 5$ kPa), and nonlinearity ($B = 12$) were selected based on previous fits of the NFSM to data from rat myocardium (Witzenburg 2014), cadaveric bladder wall (Raghupathy 2011), and cadaveric annulus fibrosus lamellae (Nagel et al. 2014). For the remainder of this article, we use the term ‘simulated experiment’ to refer specifically to the results of the simulation using the closed-form nonlinear fiber-based structural model, including results that

would be measurable experimentally (e.g. grip forces) and results that could not be measured but are available from the simulation and used for comparison with NGAIM calculations (e.g. stress or strain energy).

The simulated data were created for a cruciform sample (Figure 2) primarily aligned in one direction ($\mu = 20^\circ$) except for an inclusion with fibers of the same properties but different alignment ($\mu_{\text{inclusion}} = 80^\circ$). The results for this *in silico* problem will be presented in detail. Details as to the determination of the homogeneous subregions used in the small-strain analysis for this simulated sample are given in (Witzenburg et al. 2016). Additional studies were done on the same geometry but with variations in fiber stiffness (A), fiber nonlinearity (B), or degree of anisotropy (κ); these studies are summarized in the main article and presented in more detail in the supplemental material. The supplemental material also includes a study in which the simulated tissue was radially aligned.

Fitting NGAIM results

The simulation parameters of the closed-form nonlinear fiber-based structural model, A , B , κ and μ , were fit to the W - E curves determined for each element by NGAIM using a nonlinear simplex search, *fminsearch*, in Matlab. The small-strain analysis yields the maximum Kelvin modulus, E_K , anisotropy index, r , and preferred stiffness direction, θ which describe the linear material behavior. In brief, \mathcal{K}^1 was expressed as a second-order tensor and its eigenvalues and eigentensors allow for the determination of material stiffness, E_K , and anisotropy, r and θ (Raghupathy & Barocas 2010; Raghupathy, Witzenburg et al. 2011 describe this analysis in more detail). Here, since E_K , r , and θ were generated for the first step only, they were used to generate the initial guesses for the simulation parameters. The initial guess for the degree of anisotropy, κ , was determined from r ,

$$\kappa = \frac{r}{1 - r^2} \quad (12)$$

and the initial guess for the preferred fiber direction, μ , was set to the preferred stiffness direction, θ . The product AB can be determined directly from E_K

$$AB = \frac{2\kappa * E_K * I_0(\kappa)}{\kappa I_1(\kappa) \sqrt{4 + \frac{1}{\kappa^2}} + 2\kappa I_0(\kappa) - I_1(\kappa)} \quad (13)$$

where I_0 and I_1 are modified Bessel functions of first kind and zeroth and first orders, respectively. Since the product AB cannot be separated for small-strain data, the initial guess for B was determined from an exponential fit of Equation (11) to the equibiaxial grip force vs. grip stretch data, and then the initial guess for A was determined from

Equation (13). The exponential fit of the equibiaxial data yielded a $B = 12.9$ for the simulation.

An additional unrelated strain energy function was fit to the NGAIM results in order to test the method's flexibility. The strain energy density function utilized, the four-fiber family model, is a popular choice (Baek et al. 2007; Gleason et al. 2008; Masson et al. 2008; Wicker et al. 2008; Eberth et al. 2009; Wan et al. 2010; Di Achille et al. 2011; Sokolis et al. 2011) to describe the mechanical behavior of arteries. The strain energy function W is

$$W = \frac{c}{2}(I_1 - 2) + \sum_{k=1}^4 \frac{c_{1(k)}}{4 * c_{2(k)}} \left\{ \exp \left[c_{2(k)} * (I_{4(k)} - 1)^2 \right] - 1 \right\} \quad (14)$$

where c , $c_{1(k)}$, $c_{2(k)}$, are material parameters and the invariants I_1 and $I_{4(k)}$ are

$$I_1 = \text{tr}(C), \quad I_{4(k)} = m_{\alpha_k} \left(C m_{\alpha_k} \right) \text{ for } k = 1, 2, 3, 4 \quad (15)$$

where C is the right Cauchy–Green deformation tensor. The fiber orientations are defined in the reference configuration by the unit vectors m_{α_k} , which depend on angle α_k between the direction of the k th family of collagen fibers and the horizontal direction for the cruciform shaped sample. Following (Masson et al. 2008), although the constitutive model (14) includes four collagen-fiber families characterized by fiber angles α_k , one fiber angle was assumed to be oriented along the vertical axis ($\alpha_1 = 90^\circ$), another fiber angle was assumed to be oriented along the horizontal axis ($\alpha_2 = 0^\circ$), and the remaining fiber angles were assumed to be symmetrically oriented diagonal fibers (i.e. $\alpha_3 = \alpha$ and $\alpha_4 = -\alpha$). Additionally, fibers were assumed to have similar behaviors (i.e. $c_{1(k)} = c_1$ and $c_{2(k)} = c_2$). Consequently, from (14) and the assumptions, four parameters were fit (c , c_1 , c_2 , and α). Initial guesses for both simulations for each parameter were based on average best-fit values from (Masson et al. 2008, $c = 37$ kPa, $c_1 = 16$ kPa, $c_2 = 14$, and $\alpha = 58^\circ$), and a nonlinear simplex search, *fminsearch*, in Matlab was used to fit the four-fiber family model strain energy to the NGAIM strain energy.

Results

Stress fields

The full stress fields for the equibiaxial and right-arm-only extensions for the simulation with the inclusion ($\mu_{\text{inclusion}} = 80^\circ$) are shown for the final time step in Figures 3 and 4, respectively, alongside the stress-fields determined by NGAIM. The agreement between the stress

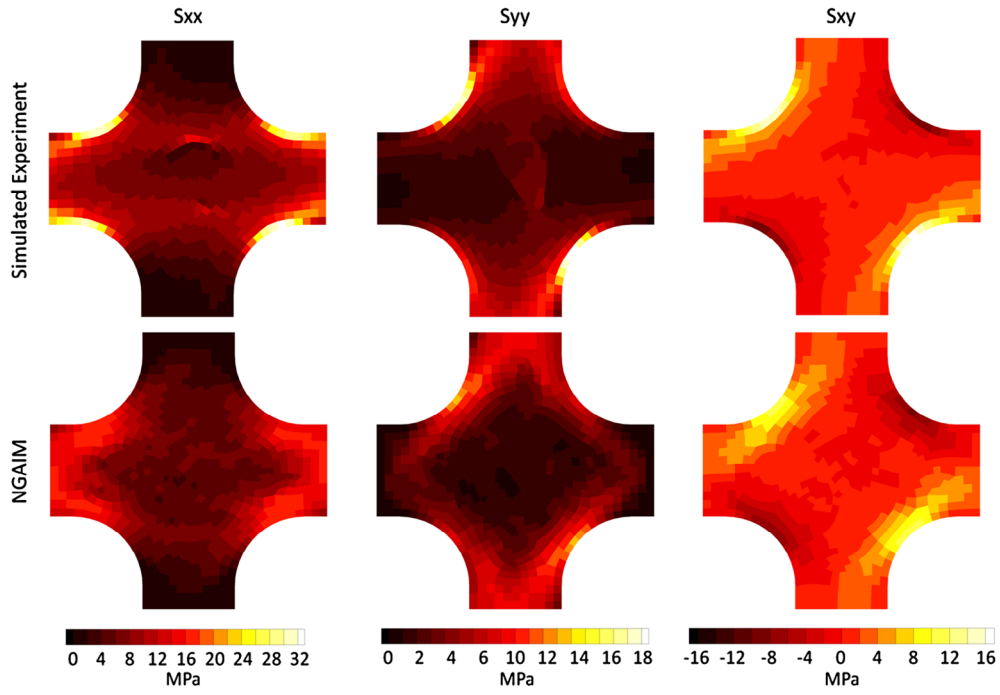


Figure 3. Stress field for the simulated sample containing an inclusion ($\mu_{\text{inclusion}} = 80^\circ$) at the end of the final time step for the equibiaxial extension.

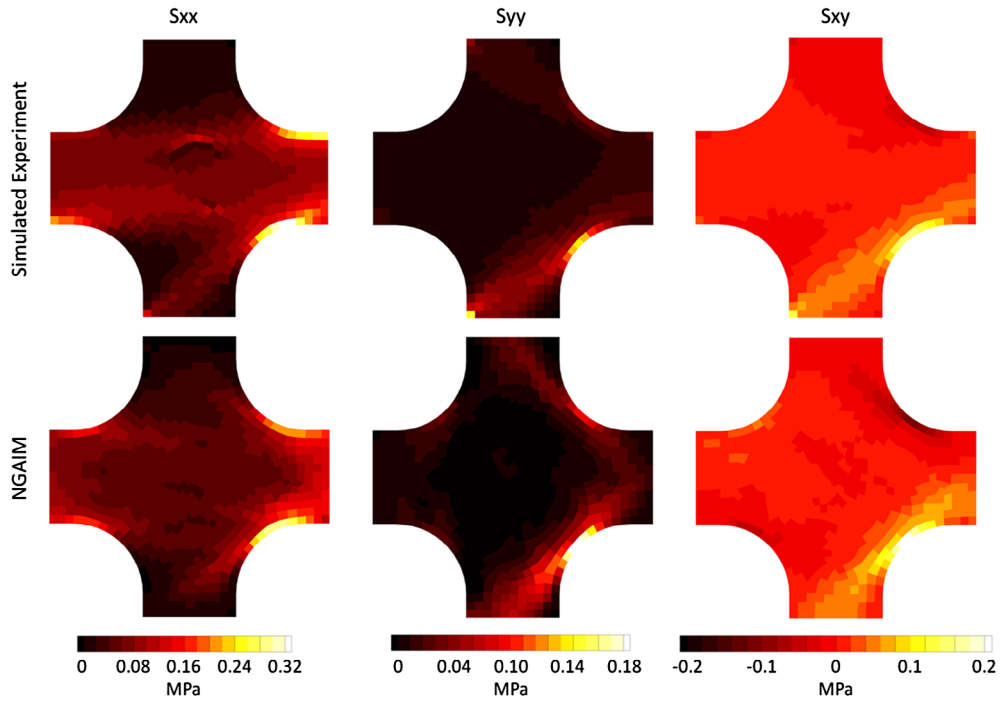


Figure 4. Stress field for the simulated sample containing an inclusion ($\mu_{\text{inclusion}} = 80^\circ$) at the end of the final time step for the right-arm-only extension.

in the simulation and the stress calculated by NGAIM is very good, especially when one considers that the NGAIM calculation is based only on the displacement fields and the grip forces.

Strain energy

The quality of the NGAIM estimate is even clearer when all time steps are considered. For clarity, two elements within

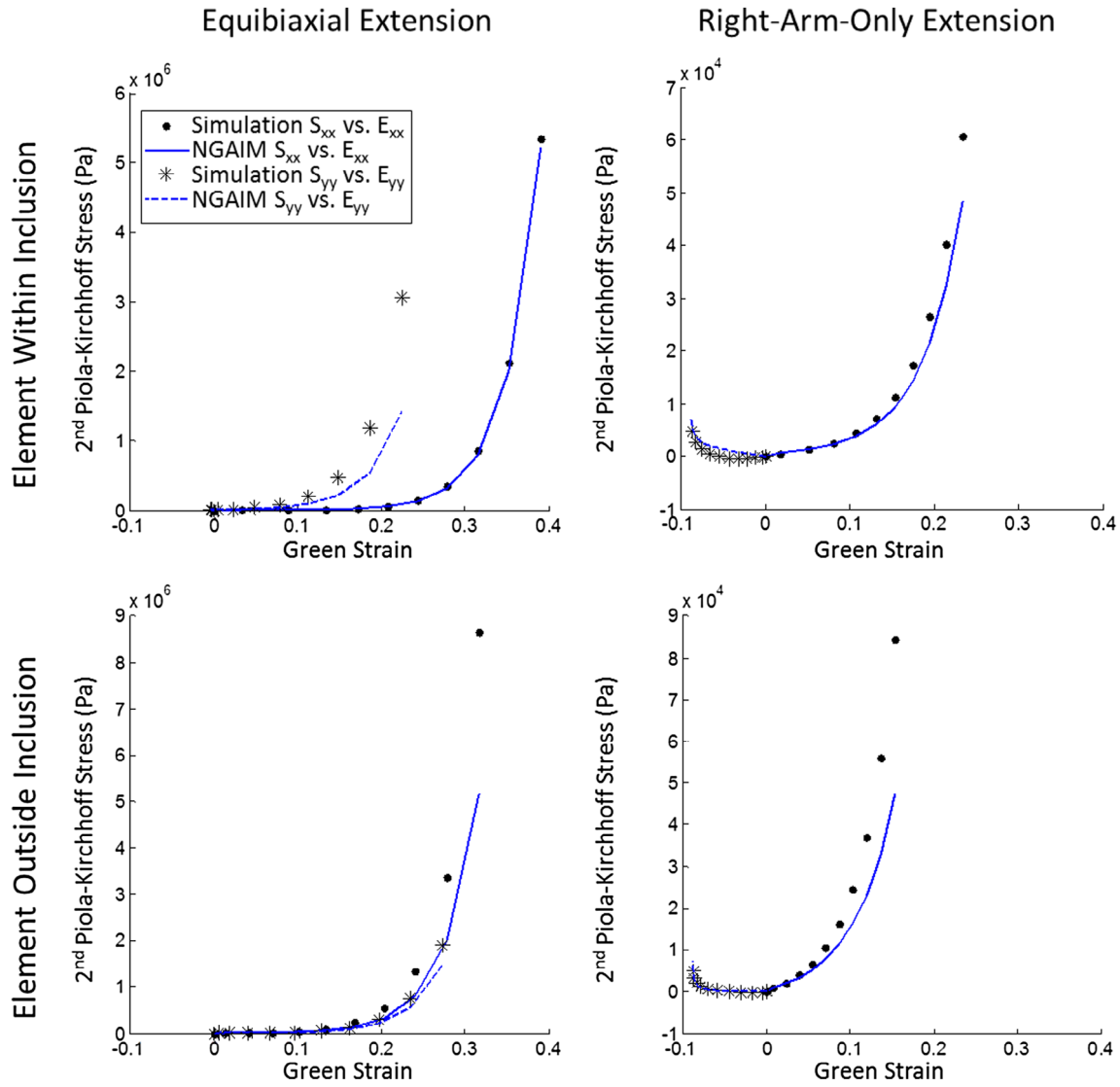


Figure 5. Stress–strain plots for representative elements. The stress and strain are plotted as (S_{xx} vs. E_{xx}) and (S_{yy} vs. E_{yy}) for elements inside and outside the inclusion (shown in Figure 2) and for both equibiaxial and right-arm-only extension. The NGAIM analysis provides a good match to the actual stress in the simulated experiment. It is important to recognize that these are not true stress–strain curves because they are not independent (i.e. E_{xx} contributes to S_{yy} and vice versa) and that the shear strain, E_{xy} , is non-zero and thus also contributes to the stress even though it is not shown in the figure.

the central region of cruciform shaped sample will be analyzed, one located in the middle of the inclusion and the other location outside of the inclusion, as marked earlier in Figure 2. Figure 5 shows the stress vs. strain (S_{xx} vs. E_{xx} and S_{yy} vs. E_{yy}) for the two elements for the equibiaxial and right-arm-only extensions. Note the high degree of nonlinearity present. NGAIM provides a good estimate of the stress in the tissue at each point for the two experimental protocols. Care must be taken when interpreting these plots, however, since the two curves are not independent and E_{xy} is not zero. A true plot of stress vs. strain would have to be six-dimensional. The dimensionality of the system can be reduced somewhat by plotting the strain energy density as a function of the three strain components.

Figure 6 shows the strain energy from the simulated experimental protocols and from NGAIM for selected elements inside and outside the inclusion (Figure 2). The plots show points in (E_{xx}, E_{yy}, E_{xy}) space, with each point representing the strain tensor in the element at a specific step of a specific protocol. The color of the point gives the strain energy at that strain state. Thus, at the origin ($E_{ij} = 0$), the strain energy is zero, and it increases as points get farther from the origin, again note the high degree of nonlinearity indicated by the log-axis. The plots for the two different elements have different points because the two elements experience different deformations, and the strain energy is different for each element because of the difference in fiber alignment. For example,

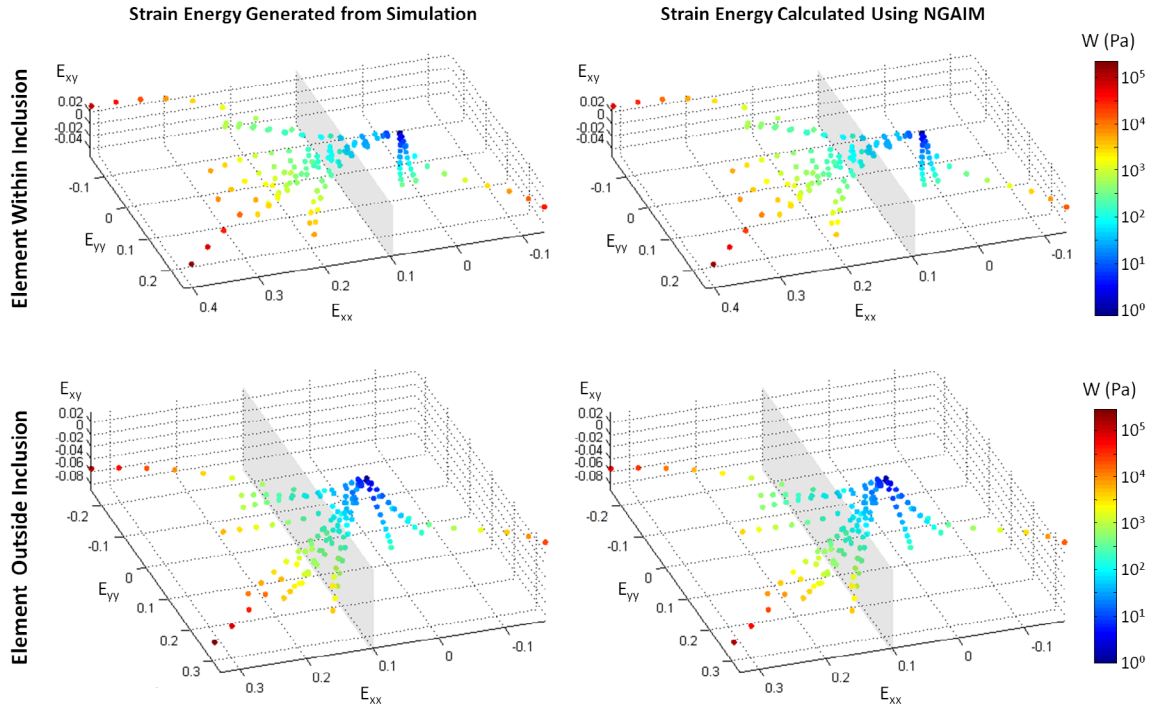


Figure 6. Strain energy (color bar) generated by the simulation and determined by NGAIM for all extensions plotted in strain space for both the element within the inclusion and the element just outside the inclusion. The strain energy in the $E_{xx} = 0.1$ plane (gray) is lower for the element within the inclusion than for the element outside the inclusion because the fibers are rotated away from the x -axis in the inclusion.

looking at points along the plane $E_{xx} = 0.1$, one can see that the strain energy is higher for the outside-inclusion case; this difference is due to the alignment of more fibers in the x -direction in the outside-inclusion case. For both elements, the simulated experiment and NGAIM analysis agree very well. The comparison is continued in Figure 7, which shows the strain energy data from Figure 6 as a scatter plot of $W_{\text{simulated}}$ vs. W_{NGAIM} where each point represents one step in one protocol. If NGAIM were estimating the stresses and thus the strain energy perfectly, all of the points would be on the line of equality. There is some deviation, especially at the high strain energy values, but the agreement is very good. The normalized root-mean-squared deviation is 2.8% for the element within the inclusion and 4.0% for the element outside the inclusion (Figure 8).

Fitting the NGAIM strain energy data set

The strain energy data set determined by NGAIM was fit by both the closed-form nonlinear fiber-based structural model (used to generate the simulation) and the four-fiber family model (unrelated strain energy function). The fits for both the closed-form nonlinear fiber-based structural model and the four-fiber family model are shown in Figure 8. The normalized root-mean-square deviation (NRMSD) indicates the closed-form nonlinear

fiber-based structural model better fit the strain energy data set determined by NGAIM; this result was expected since that model was used to generate the simulated experiments. The best-fit four-fiber family model parameters were $c = 2.1e^{-11}$ kPa, $c_1 = 17.5$ kPa, $c_2 = 6.7e^{-3}$ kPa, and $\alpha = 28.1^\circ$ for the element within the inclusion and $c = 1.2e^{-7}$ kPa, $c_1 = 16.6$ kPa, $c_2 = 9.6e^{-3}$ kPa, and $\alpha = 21.8^\circ$ for the element outside the inclusion. Even though the four-fiber family model is different from the closed-form nonlinear fiber-based structural model, the strain energies from the four-fiber family model are in fairly good agreement with the simulated experiment over a very broad range. This result is important because in a real experiment, one would not know the best constitutive form *a priori*.

For the nonlinear fiber-based structural model, the fitted parameters are compared to those utilized to generate the simulations in Figure 9. If the fitted parameters matched those used to generate the simulation then the degree of anisotropy, fiber stiffness, and fiber nonlinearity graphs would be white. The fitted NGAIM results were able to recapture the prescribed simulation parameters well. Regions near the grips and edges experience smaller ranges in strain due to sample geometry, so the NGAIM fitted estimates are less accurate there. There is very good agreement between the fiber orientation prescribed and the fiber orientation recovered both within

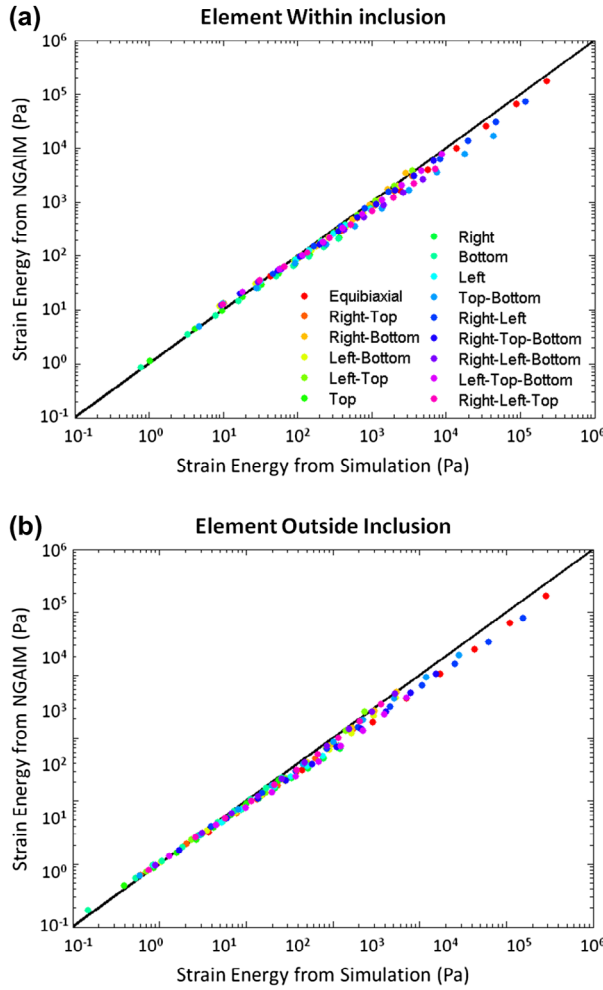


Figure 7. Strain energy determined using the NGAIM vs. the strain energy generated by the simulation for all steps (dots) of each experimental protocol (colors) for the element within the inclusion (a) and the element just outside of the inclusion (b). The diagonal black line indicates a perfect prediction.

the inclusion and at the inclusion border. In addition, the degree of anisotropy ($\kappa_{\text{simulation}} = 1.5$), fiber stiffness ($A_{\text{simulation}} = 0.005$ Mpa), and fiber nonlinearity ($B_{\text{simulation}} = 12$) were well recovered, particularly in the central region of the sample. An additional fit of the closed-form nonlinear fiber-based structural model was performed for the simulation with varied alignment in which the initial value of B was set to 1 and to 24 in order to gauge the influence of initial guess on the final fit. When the initial value of B was set to 1 the NRMSD was 2.9 and 4.1% and when it was set to 24 the NRMSD was 2.7 and 4.1%, for the element within the inclusion and the element outside the inclusion, respectively. Thus, large variations in the initial guess for B caused at most an increase in NRMSD of only 0.1%.

Additional simulations on the cruciform sample with a central triangular shaped inclusion that varied

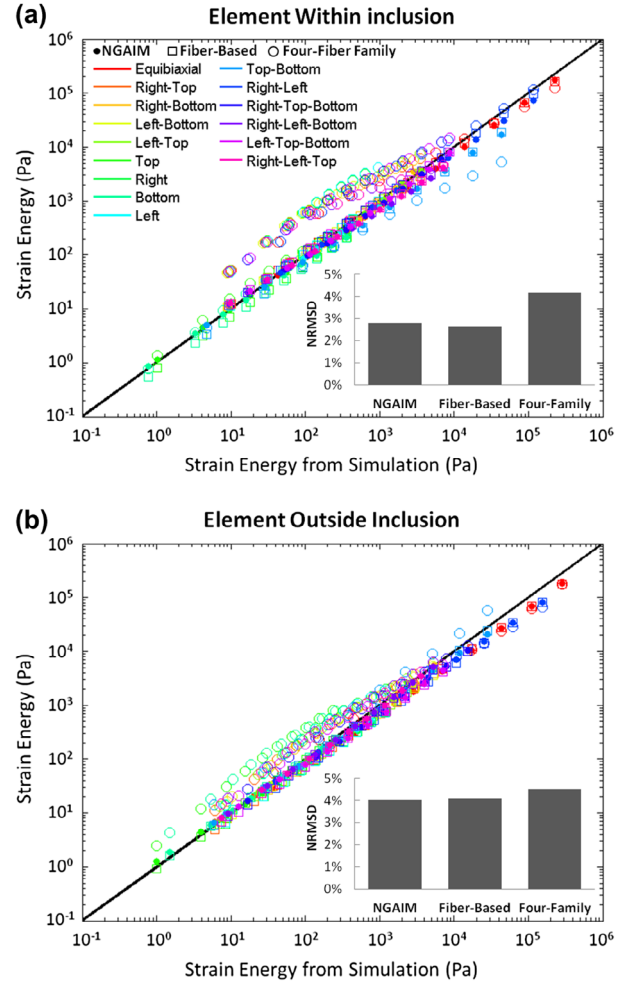


Figure 8. Strain energy determined using NGAIM (colored dots), determined by the fit of the closed-form nonlinear fiber-based structural model to the NGAIM results (colored squares), and determined by the fit of the four-fiber family model to the NGAIM results (colored circles) vs. the strain energy generated by the simulation for all biaxial extensions for the element within the inclusion (a) and the element just outside of the inclusion (b). The diagonal black line indicates a perfect prediction. Inset bar graphs indicate the NRMSD associated with both NGAIM and the fits.

from the bulk sequentially in strength of alignment ($\kappa_{\text{bulk}} = 1.5$ and $\kappa_{\text{inclusion}} = 6.0$), stiffness ($A_{\text{bulk}} = 5$ kPa and $A_{\text{inclusion}} = 20$ kPa), and nonlinearity ($B_{\text{bulk}} = 12$ and $B_{\text{inclusion}} = 48$) were performed. The closed-form nonlinear fiber-based structural model parameters determined by fitting the stress-strain behavior predicted by the NGAIM method compared with the parameters used to generate the simulated sample are shown for each additional simulation in Figure 10. In all cases the NGAIM method performed well. The poorest match of NGAIM to the simulation strain energy occurred in the element within the inclusion for the simulation in which nonlinearity varied between the bulk and inclusion.

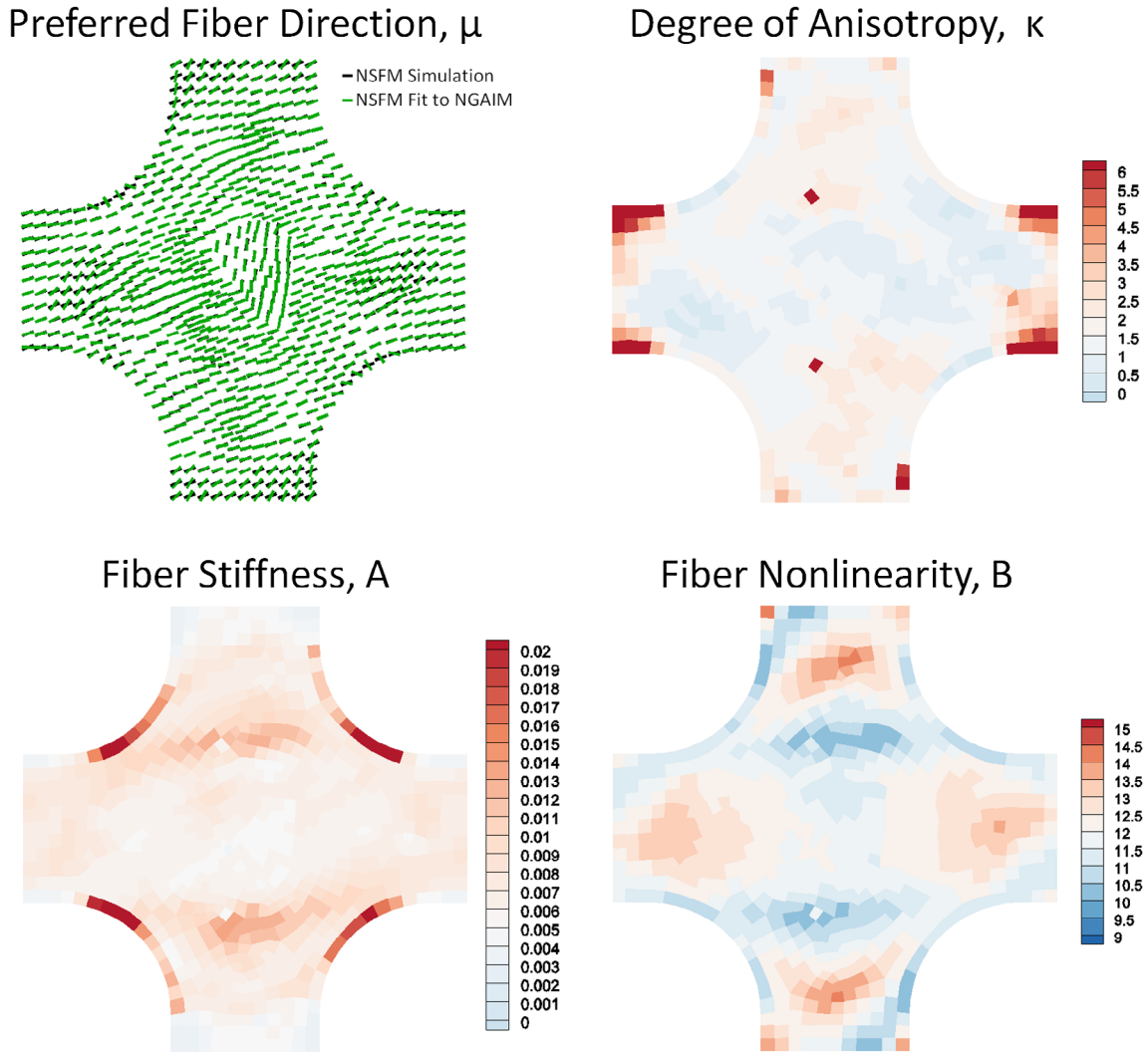


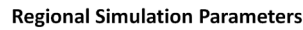
Figure 9. Simulation parameters recovered by fitting the W -strain behavior predicted by NGAIM with the closed-form nonlinear fiber-based structural model compared with the parameters used to generate the simulated sample. The preferred fiber direction prescribed is in black and the one recovered by NGAIM is in green. All other parameters are shown on scales which place the original values at the center (i.e. white denotes a perfect match between fitted parameters and values used to generate the simulation).

Discussion

The key to extending GAIM was to discretize each nonlinear curve into many short linear segments, an approach which allows for the consideration of the nonlinear force-displacement curves without sacrificing the tremendous efficiency advantage of the linear model. Piecewise linear representation of a nonlinear function is straight forward in one dimension, but implementation in the context of a two-dimensional large-deformation experiment is not trivial. The NGAIM method generates a set of local elasticity tensors describing the material behavior of a particular element within the sample for part of one test protocol. Multiplying each tensor by the strain measured experimentally in that region during that portion of the testing protocol yields an incremental stress. By combining all the incremental stresses calculated over all

segments of all protocols for a particular region, a set of stress-strain curves was determined from which a unique strain energy density data set was generated.

The *in silico* results for NGAIM show good agreement between the strain energy and full-field stress recovered by NGAIM and that generated by the closed-form nonlinear fiber-based structural model. In particular, as shown in Figures 5–7, the behavior of the sample throughout testing, and not just at its endpoint, is captured. The closed-form nonlinear fiber-based structural model parameters utilized to generate the simulation were well-recovered, as shown in Figure 9, particularly within the inclusion and at its border. For the other studies on strength of anisotropy, stiffness, and nonlinearity NGAIM performed well generally. For all simulations, NGAIM exhibited larger errors at larger strain levels, likely due to the exponential nature of the stress-strain behavior of the tissue. One potential



at the grip. A tester that utilizes multiple load cells (like that of Khalsa et al. 1996; Flynn et al. 1998) would also allow for more detailed force measurements at the sample boundary and the direct imposition of shear. As indicated by Sacks (2014), however, when asymmetric loading is introduced in this manner during planar biaxial testing, there is the potential for out-of-plane deformation. Sacks suggests rotation of the test specimen such that the fiber and cross-fiber directions do not coincide with the test machine axes and the use of rotating carriages to induce shear and avoid wrinkling. A multiaxial tester like that of Nielsen and colleagues (Malcolm et al. 2002; Nielsen et al. 2002) is a more involved, sophisticated approach to the introduction of shear. It allows for a broader strain space to be imposed on each region of the sample while controlling against out-of-plane deformation. In addition, though it is more experimentally demanding, the Nielsen apparatus allows for more detailed measurement of force at the sample boundary. The series of biaxial experimental protocols poses practical challenges to biaxial testing since the potential for damage or irrecoverable deformation increases with the number of protocols performed.

However, as NGAIM relies so heavily on step 1 of the various protocols it becomes even more crucial that the matrix problem for step 1 is grossly over-determined. Sensitivity to noise, particularly at the low force levels measured, must be minimized. Therefore, we have selected to continue using the full loading scheme. In addition, we have opted to use a deformation gradient jump technique in order to guide partitioning (Witzenburg et al. 2016). So, partitioning choices for the first step are based on the full nonlinear behavior of the tissue. Finally, the method to determine an appropriate step size was strongly influenced by the need for accuracy in step 1. When determining step size, the need to capture as much of the mechanical behavior of the tissue as possible within a single step must be balanced with the need to fit the behavior linearly, as discussed in Appendix 1.

The NGAIM method builds on the work of Raghupathy and Barocas (2010) adding the capacity to analyze nonlinear samples to the original method for heterogeneous, anisotropic samples. It uses experimental testing results from biaxial testing, allowing for the tissue specimen to be placed in a wide variety of strain states including states experienced physiologically. It does not require a fully integrated finite element model, and in the large-strain analysis it can be parallelized to maximize efficiency. Thus, it can be run on a standard computer (vs. a supercomputer) in a matter of minutes to hours. Finally it utilizes a subdomain partitioning technique to partition the sample into homogenous subregions allowing for the characterization of heterogeneous samples. The main advantage of the NGAIM method, however, is its flexibility. NGAIM generates a data-driven strain energy field for each element within the sample domain. Once this strain energy data set is determined, *any* strain energy function can be used to describe the element's material behavior. Fitting a strain energy function to this data set is simple and quick, allowing one to compare various strain energy functions easily and select different functions for different regions, if appropriate. In this work, a closed-form structural model of planar fibrous tissue mechanics developed by Raghupathy and Barocas (2009), as well as a version of the four-fiber family model (Masson et al. 2008) were fit to the strain energy fields. The ability of NGAIM to generate a full strain energy field makes it extremely versatile and efficient.

Disclosure statement

No potential conflict of interest was reported by the authors.

Funding

This work was supported by NIH [R01-EB005813]. CMW was supported by a University of Minnesota Doctoral Dissertation

Fellowship. Computations were made possible by a resource grant from the Minnesota Supercomputing Institute.

References

- Baek S, Gleason RL, Rajagopal KR, Humphrey JD. 2007. Theory of small on large: potential utility in computations of fluid–solid interactions in arteries. *Comput Methods Appl Mech Eng.* 196:3070–3078.
- Bischoff JE. 2004. Static indentation of anisotropic biomaterials using axially asymmetric indenters – a computational study. *J Biomech Eng.* 126:498–505.
- Boyce BL, Grazier JM, Jones RE, Nguyen TD. 2008. Full-field deformation of bovine cornea under constrained inflation conditions. *Biomaterials.* 29:3896–3904.
- Chai C-K, Akyildiz AC, Speelman L, Gijzen FJH, Oomens CWJ, van Sambeek MRHM, van der Lugt A, Baaijens FPT. 2013. Local axial compressive mechanical properties of human carotid atherosclerotic plaques-characterisation by indentation test and inverse finite element analysis. *J Biomech.* 46:1759–1766.
- Chai C-K, Speelman L, Oomens CWJ, Baaijens FPT. 2014. Compressive mechanical properties of atherosclerotic plaques-indentation test to characterise the local anisotropic behaviour. *J Biomech.* 47:784–792.
- Clayton EH, Okamoto RJ, Bayly PV. 2013. mechanical properties of viscoelastic media by local frequency estimation of divergence-free wave fields. *J Biomech Eng.* 135:021025.
- Costa KD, Yin FC. 1999. Analysis of indentation: implications for measuring mechanical properties with atomic force microscopy. *J Biomech Eng.* 121:462–471.
- Cox MAJ, Driessen NJB, Boerboom RA, Bouten CVC, Baaijens FPT. 2008. Mechanical characterization of anisotropic planar biological soft tissues using finite indentation: experimental feasibility. *J Biomech.* 41:422–429.
- Cox MAJ, Kortsmit J, Driessen N, Bouten CVC, Baaijens FPT. 2010. Tissue-engineered heart valves develop native-like collagen fiber architecture. *Tissue Eng Part A.* 16:1527–1537.
- Demer LL, Yin FC. 1983. Passive biaxial mechanical properties of isolated canine myocardium. *J Physiol.* 339:615–630.
- Di Achille P, Celi S, Di Puccio F, Forte P. 2011. Anisotropic AAA: computational comparison between four and two fiber family material models. *J Biomech.* 44:2418–2426.
- Eberth JE, Taucer AI, Wilson E, Humphrey JD. 2009. Mechanics of carotid arteries in a mouse model of Marfan syndrome. *Ann Biomed Eng.* 37:1093–1104.
- Ehman RL, Glaser kJ, Manduca A. 2012. Review of MR elastography applications and recent developments. *J Magn Reson Imaging.* 36:757–774.
- Flynn DM, Peura GD, Grigg P, Hoffman AH. 1998. A finite element based method to determine the properties of planar soft tissue. *J Biomech Eng.* 120:202–210.
- Flynn C, Taberner A, Nielsen P. 2011. Modeling the mechanical response of *in vivo* human skin under a rich set of deformations. *Ann Biomed Eng.* 39:1935–1946.
- Flynn C, Taberner AJ, Nielsen PMF, Fels S. 2013. Simulating the three-dimensional deformation of *in vivo* facial skin. *J Mech Behav Biomed Mater.* 28:484–494.
- Fung YC. 1993. *Biomechanics: mechanical properties of living tissues.* 2nd ed. New York (NY): Springer Science & Business Media.

- Ghaemi H, Behdian K, Spence AD. 2009. *In vitro* technique in estimation of passive mechanical properties of bovine heart. Part I. Experimental techniques and data. *Med Eng Phys*. 31:76–82.
- Gleason RL, Dye WW, Wilson E, Humphrey JD. 2008. Quantification of the mechanical behavior of carotid arteries from wild-type, dystrophin-deficient, and sarcoglycan- δ knockout mice. *J Biomech*. 41:3213–3218.
- Goenezen S, Barbone P, Oberai AA. 2011. Solution of the nonlinear elasticity imaging inverse problem: the incompressible case. *Comput Methods Appl Mech Eng*. 200:1406–1420.
- Goenezen S, Dord J-F, Sink Z, Barbone PE, Jiang J, Hall TJ, Oberai AA. 2012. Linear and nonlinear elastic modulus imaging: an application to breast cancer diagnosis. *IEEE Trans Med Imaging*. 31:1628–1637.
- Gokhale NH, Barbone PE, Oberai AA. 2008. Solution of the nonlinear elasticity imaging inverse problem: the compressible case. *Inverse Prob*. 24:045010.
- Greenleaf JF, Fatemi M, Insana M. 2003. Selected methods for imaging elastic properties of biological tissues. *Annu Rev Biomed Eng*. 5:57–78.
- Holzapfel GA. 2000. *Nonlinear solid mechanics: a continuum approach for engineering*. 1st ed. West Sussex: Wiley.
- Holzapfel GA, Gasser TC, Ogden RW. 2000. A new constitutive framework for arterial wall mechanics and a comparative study of material models. *J Elast*. 61:1–48.
- Huang C-Y, Wang VM, Pawluk RJ, Bucchieri JS, Levine WN, Bigliani LU, Mow VC, Flatow EL. 2005. Inhomogeneous mechanical behavior of the human supraspinatus tendon under uniaxial loading. *J Orthop Res*. 23:924–930.
- Hughes TJR, Pister KS. 1978. Consistent linearization in mechanics of solids and structures. *Comput Struct*. 8:391–397.
- Humphrey JD. 1999. An evaluation of pseudoelastic descriptors used in arterial mechanics. *J Biomech Eng*. 121:259–262.
- Humphrey JD. 2002. *Cardiovascular solid mechanics: cells, tissues, and organs*. New York (NY): Springer Science & Business Media.
- Humphrey JD, Halperin HR, Yin FCP. 1991. Small indentation superimposed on a finite equibiaxial stretch: implications for cardiac mechanics. *J Appl Mech*. 58:1108–1111.
- Karduna AR, Halperin HR, Yin FC. 1997. Experimental and numerical analyses of indentation in finite-sized isotropic and anisotropic rubber-like materials. *Ann Biomed Eng*. 25:1009–1016.
- Khalsa PS, Hoffman AH, Grigg P. 1996. Mechanical states encoded by stretch-sensitive neurons in feline joint capsule. *J Neurophysiol*. 76:175–187.
- Kroon M, Holzapfel GA. 2008. Estimation of the distributions of anisotropic, elastic properties and wall stresses of saccular cerebral aneurysms by inverse analysis. *Proc R Soc A Math Phys Eng Sci*. 464:807–825.
- Lake SP, Miller KS, Elliott DM, Soslowsky LJ. 2009. Effect of fiber distribution and realignment on the nonlinear and inhomogeneous mechanical properties of human supraspinatus tendon under longitudinal tensile loading. *J Orthop Res*. 27:1596–1602.
- Lake SP, Miller KS, Elliott DM, Soslowsky LJ. 2010. Tensile properties and fiber alignment of human supraspinatus tendon in the transverse direction demonstrate inhomogeneity, nonlinearity, and regional isotropy. *J Biomech*. 43:727–732.
- Lu J, Zhao X. 2009. Pointwise identification of elastic properties in nonlinear hyperelastic membranes – Part I: theoretical and computational developments. *J Appl Mech*. 76:061013.
- Malcolm DTK, Nielsen PMF, Hunter PJ, Charette PG. 2002. Strain measurement in biaxially loaded inhomogeneous, anisotropic elastic membranes. *Biomech Model Mechanobiol*. 1:197–210.
- Manduca A, Oliphant TE, Dresner MA, Mahowald JL, Kruse SA, Amromin E, Felmlee JP, Greenleaf JF, Ehman RL. 2001. Magnetic resonance elastography: non-invasive mapping of tissue elasticity. *Med Image Anal*. 5:237–254.
- Masson I, Boutouyrie P, Laurent S, Humphrey JD, Zidi M. 2008. Characterization of arterial wall mechanical behavior and stresses from human clinical data. *J Biomech*. 41:2618–2627.
- Nagel TM, Hadi MF, Claeson AA, Nuckley DJ, Barocas VH. 2014. Combining displacement field and grip force information to determine mechanical properties of planar tissue with complicated geometry. *J Biomech Eng*. 136:114501.
- Nielsen PMF, Malcolm DTK, Hunter PJ, Charette PG. 2002. Instrumentation and procedures for estimating the constitutive parameters of inhomogeneous elastic membranes. *Biomech Model Mechanobiol*. 1:211–218.
- Novak VP, Yin FCP, Humphrey JD. 1994. Regional mechanical properties of passive myocardium. *J Biomech*. 27:403–412.
- Ogden RW. 1984. Incremental elastic deformations. In: *Non-linear elastic deform*. New York (NY): Wiley; p. 328–478.
- Ophir J, Cespedes I, Garra B, Ponnekanti H, Huang Y, Maklad N. 1996. Elastography: Ultrasonic imaging of tissue strain and elastic modulus *in vivo*. *Eur J Ultrasound*. 3:49–70.
- Pasta S, Phillippi JA, Gleason TG, Vorp DA. 2012. Effect of aneurysm on the mechanical dissection properties of the human ascending thoracic aorta. *J Thorac Cardiovasc Surg*. 143:460–467.
- Pedrigi RM, David G, Dziezyc J, Humphrey JD. 2007. Regional mechanical properties and stress analysis of the human anterior lens capsule. *Vision Res*. 47:1781–1789.
- Perumpail RB, Levitsky J, Wang Y, Lee VS, Karp J, Jin N, Yang GY, Bolster BD, Shah S, Zuehlsdorff S, et al. 2012. MRI-guided biopsy to correlate tissue specimens with MR elastography stiffness readings in liver transplants. *Acad Radiol*. 19:1121–1126.
- Raghupathy R. 2011. *Form from function: generalized anisotropic inverse mechanics for soft tissues*. Twin Cities: University of Minnesota.
- Raghupathy R, Barocas VH. 2009. A closed-form structural model of planar fibrous tissue mechanics. *J Biomech*. 42:1424–1428.
- Raghupathy R, Barocas VH. 2010. Generalized anisotropic inverse mechanics for soft tissues. *J Biomech Eng*. 132:081006.
- Raghupathy R, Witzenburg CM, Lake SP, Sander EA, Barocas VH. 2011. Identification of regional mechanical anisotropy in soft tissue analogs. *J Biomech Eng*. 133:091011.
- Sacks MS. 2014. Engineering a method for planar biaxial mechanical testing that includes in-plane shear. *J Biomech Eng*. 121:551–555.
- Sacks MS, Chuong CJ. 1993. Biaxial mechanical properties of passive right ventricular free wall myocardium. *J Biomech Eng*. 115:202–205.
- Saravanan U, Baek S, Rajagopal KR, Humphrey JD. 2006. On the deformation of the circumflex coronary artery during inflation tests at constant length. *Exp Mech*. 46:647–656.

- Schulze-Bauer CAJ, Regitnig P, Holzapfel GA. 2002. Mechanics of the human femoral adventitia including the high-pressure response. *Am J Physiol Heart Circ Physiol.* 282:H2427–H2440.
- Seshaiyer P, Humphrey JD. 2003. A sub-domain inverse finite element characterization of hyperelastic membranes including soft tissues. *J Biomech Eng.* 125:363–371.
- Sinkus R, Tanter M, Bercoff J, Siegmann K, Pernot M, Athanasiou A, Fink M. 2008. Potential of MRI and ultrasound radiation force in elastography: applications to diagnosis and therapy. *Proc IEEE.* 96:490–499.
- Sokolis DP, Boudoulas H, Karayannacos PE. 2008. Segmental differences of aortic function and composition: clinical implications. *Hell J Cardiol.* 49:145–154.
- Sokolis DP, Sassani S, Kritharis EP, Tsangaris S. 2011. Differential histomechanical response of carotid artery in relation to species and region: mathematical description accounting for elastin and collagen anisotropy. *Med Biol Eng Comput.* 49:867–879.
- Szczesny SE, Peloquin JM, Cortes DH, Kadlowec JA, Soslowsky LJ, Elliott DM. 2012. Biaxial tensile testing and constitutive modeling of human supraspinatus tendon. *J Biomech Eng.* 134:021004.
- Thomopoulos S, Marquez JP, Weinberger B, Birman V, Genin GM. 2006. Collagen fiber orientation at the tendon to bone insertion and its influence on stress concentrations. *J Biomech.* 39:1842–1851.
- Tönük E, Silver-Thorn MB. 2003. Nonlinear elastic material property estimation of lower extremity residual limb tissues. *IEEE Trans Neural Syst Rehabil Eng.* 11:43–53.
- Tweten DJ, Okamoto RJ, Schmidt JL, Garbow JR, Bayly PV. 2015. Estimation of material parameters from slow and fast shear waves in an incompressible, transversely isotropic material. *J Biomech.* 48:4002–4009.
- Tyagi M, Goenezen S, Barbone PE, Oberai AA. 2014. Algorithms for quantitative quasi-static elasticity imaging using force data. *Int J Numer Method Biomed Eng.* 30:1421–1436.
- Vande Geest JP, Sacks MS, Vorp DA. 2006. The effects of aneurysm on the biaxial mechanical behavior of human abdominal aorta. *J Biomech.* 39:1324–1334.
- Wan W, Yanagisawa H, Gleason RL. 2010. Biomechanical and microstructural properties of common carotid arteries from fibulin-5 null mice. *Ann Biomed Eng.* 38:3605–3617.
- Wicker BK, Hutchens HP, Wu Q, Yeh AT, Humphrey JD. 2008. Normal basilar artery structure and biaxial mechanical behaviour. *Comput Methods Biomech Biomed Eng.* 11:539–551.
- Witzenburg CM, Raghupathy R, Kren SM, Taylor DA, Barocas VH. 2012. Mechanical changes in the rat right ventricle with decellularization. *J Biomech.* 45:842–849.
- Witzenburg CM. 2014. Coupled theoretical and experimental methods to characterize heterogeneous, anisotropic, nonlinear materials: application to cardiovascular tissues. Twin Cities: University of Minnesota.
- Witzenburg CM, Dhume RY, Lake SP, Barocas VH. 2016. Automatic segmentation of mechanically inhomogeneous tissues based on deformation gradient jump. *IEEE Trans Med Imaging.* 35:29–41.
- Zhao X, Chen X, Lu J. 2009. Pointwise identification of elastic properties in nonlinear hyperelastic membranes – Part II: experimental validation. *J Appl Mech.* 76:061014.
- Zhao X, Raghavan ML, Lu J. 2011. Identifying heterogeneous anisotropic properties in cerebral aneurysms: a pointwise approach. *Biomech Model Mechanobiol.* 10:177–189.

Appendix 1. Step size determination

In order to fit the GAIM Method to the data in a stepwise manner, first an appropriate step size must be determined. To determine step size, lines were fit to the force vs. time curves for each biaxial extension, as shown in Figure A.1 for the simulated sample containing an inclusion with fiber orientation different from the bulk (Figure 2). The coefficient of determination, r -squared, was used to evaluate the linear fit. If the slope of the data was sufficiently non-zero (in this case, $|\text{slope}| > 5.6e - 7$), then the r -squared value was calculated. The minimum r -squared value was calculated for all steps and all protocols and if it was less than 0.9 (the level at which a stepwise linear approximation was deemed appropriate), step size was reduced. For the simulation, a step size of 0.5 s was selected and the minimum r -squared value calculated for all steps and all protocols was 0.9044. The displacement fields for the sample at the end of each step for the equibiaxial and right-arm-only extensions are shown in Figures A.2(a) and (b), respectively.

The step size is an important specification when implementing NGAIM. The closed-form nonlinear fiber-based structural model has nearly infinite time resolution, so any step size can be accommodated. But experimentally, there are practical limits that restrict how much step size can be reduced. The resolution and data acquisition rate of available load cells must be considered. In addition, if full-field displacement is determined optically, both frame rate and spatial resolution must be considered. The maximum displacement of a node in any step of the representative simulation is 0.09 mm, which assuming a spatial resolution similar to that achieved previously (Raghupathy et al. 2011; Witzenburg et al. 2012), is equivalent to approximately 8 pixels, a value that is reasonable given the image analysis and strain tracking methods utilized experimentally (Raghupathy 2011; Raghupathy et al. 2011). The measurement of loads at low levels requires load cells with excellent resolution and accuracy. In addition, precise levels of preload and preconditioning must be applied carefully. For experimental data obtained using the biaxial tester (Instron¹ load cells (JR3 Inc. (Nagel et al. 2014)) and digital camera (Cannon, 24 fps, 1080p HD resolution) available at the University of Minnesota, a step size of 0.5 s is reasonable.

Note

1. Available at the University of Minnesota <http://bme.umn.edu/research/tissuemech.html>

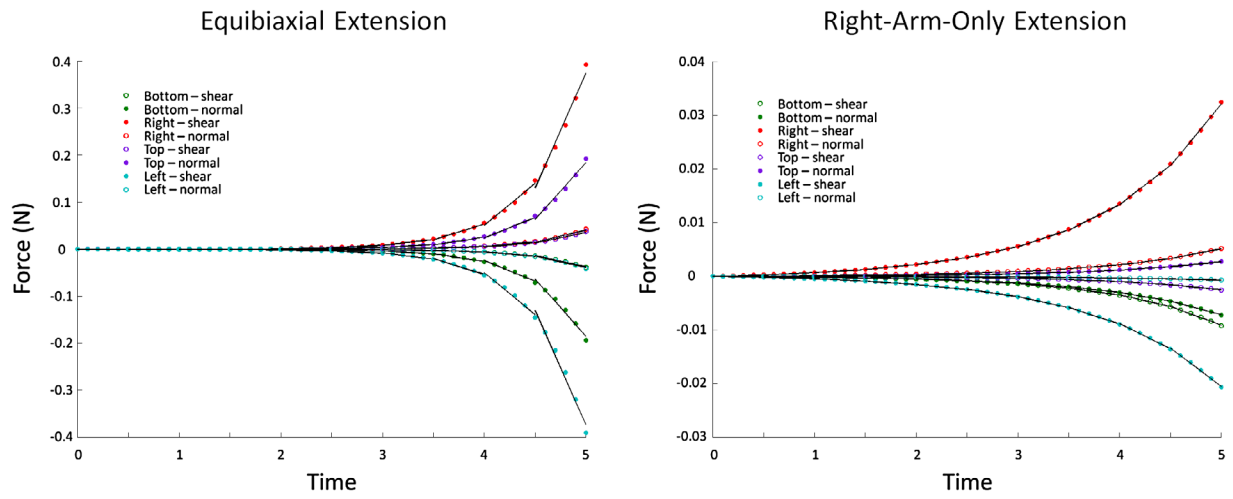


Figure A.1. Final step size fits for the equibiaxial and right-arm-only extensions for the simulated sample containing an inclusion in which the fiber orientation is rotated, shown in Figure 2. Ten steps were utilized to describe the force behavior. Time is in units of seconds.

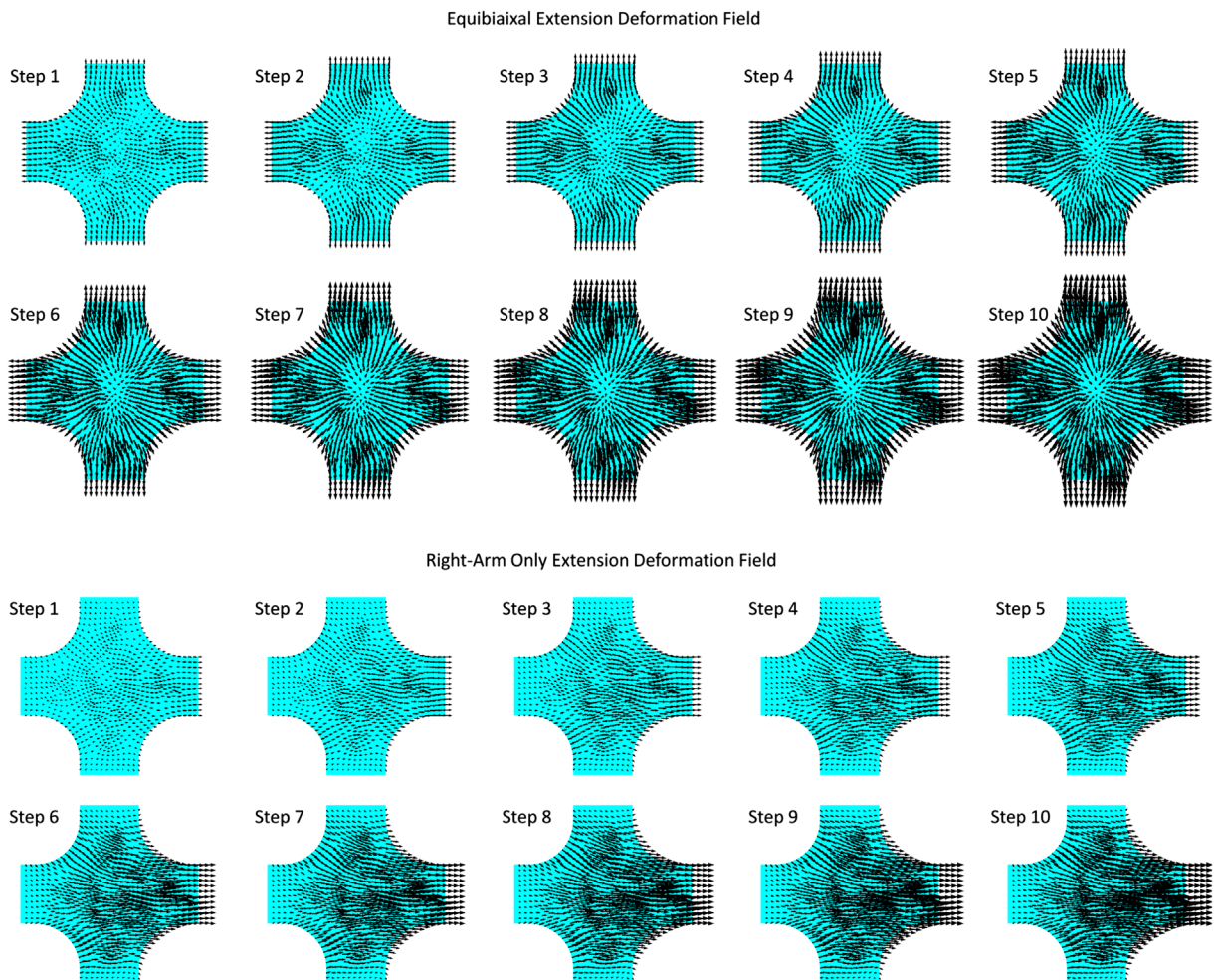


Figure A.2. Displacement field for equibiaxial and right-arm-only extensions for the representative simulation at the end of each step.